

Article

The Influence of the Galactic Bar on the Dynamics of Globular Clusters

Roman Tkachenko ^{1,*}, Vladimir Korchagin ^{1,†}, Anna Jmailova ^{2,†}, Giovanni Carraro ^{3,†} and Boris Jmailov ⁴

¹ Institute of Physics, Southern Federal University, Stachki Avenue 124, 344090 Rostov-on-Don, Russia; vkorchagin@sfedu.ru

² Physical Faculty, Southern Federal University, Zorge Street 5, 344090 Rostov-on-Don, Russia; zhmailova@sfedu.ru

³ Dipartimento di Fisica e Astronomia Galileo Galilei, Università degli Studi di Padova, Vicolo Osservatorio 3, I-35122 Padova, Italy; giovanni.carraro@unipd.it

⁴ Institute of High Technologies and Piezotechnics, Southern Federal University, 10 Milchakova Street, 344090 Rostov-on-Don, Russia; bbzhmaylov@sfedu.ru

* Correspondence: rtkachenko@sfedu.ru

† These authors contributed equally to this work.

Abstract: We make use of recent estimates for the parameters of the Milky Way's halo globular clusters and study the influence of the galactic bar on the dynamics of these clusters by computing their orbits. We use both an axisymmetric and non-axisymmetric galactic potentials, which include the rotating elongated bar/bulge structure. We account for observational errors both in the positions and in the velocities of the globular clusters and explore the influence of the bar on clusters' evolution. This is contained in the angular momentum–total energy plane, (L_z, E) , which is widely exploited as an indicator of the groups of globular clusters that originated from the same accretion event. Particular attention is devoted to the Gaia-Sausage/Enceladus and Pontus structures identified recently as two independent accretion events. Our study shows that it is not possible to identify GSE and Pontus as different merger events.

Keywords: milky way; globular clusters; galactic bar; numerical simulation; galactic dynamics; galactic halo



Citation: Tkachenko, R.; Korchagin, V.; Jmailova, A.; Carraro, G.; Jmailov, B. The Influence of the Galactic Bar on the Dynamics of Globular Clusters. *Galaxies* **2023**, *1*, 15. <https://doi.org/10.3390/galaxies11010026>

Academic Editor: Roberta Humphreys

Received: 19 December 2022

Accepted: 1 February 2023

Published:

Publisher's Note: MDPI stays neutral with regard to jurisdictional claims in published maps and institutional affiliations.



Copyright: © 2023 by the authors. Licensee MDPI, Basel, Switzerland. This article is an open access article distributed under the terms and conditions of the Creative Commons Attribution (CC BY) license (<https://creativecommons.org/licenses/by/4.0/>).

1. Introduction

Modern cosmological models predict that the halo of our galaxy was formed by and evolved through the continuous accretion and disruption of star clusters, small satellite galaxies [1,2], and gas accretion events [3]. Our galaxy, the Milky Way, is a unique and excellent laboratory [4] in which to investigate how this process occurred by studying examples of such accretions, such as the ongoing merging process of the Sagittarius dwarf galaxy [5]; echoes of the past accretion events, e.g., Gaia-Sausage/Enceladus (GSE) at $z \sim 2$ [4,6]; or even the first fall beginnings of the Magellanic Clouds [7]. As a result of such mergers, the halo of Milky Way galaxy, or at least part of it, was built with the products of such accretions as the stellar streams or the globular clusters of extra-galactic origin.

Our Galaxy consists of a few subsystems—a galactic halo, thick and the thin disks and an elongated bar/bulge [8,9]—that have stars with different spatial distributions, velocity dispersions and chemical compositions. Moreover, even within one subsystem, a few subgroups that have different origins can be often distinguished [4,10,11]. According to Naidu et al. [4], for example, most of the stars in the inner halo of the Milky Way seem to be associated with the GSE accretion event. A comprehensive study of traces of the past mergers is important, therefore, to understand how our Galaxy was formed and how it will evolve in the future.

The Gaia mission [12–15], with its accurate data on the coordinates, velocities and metallicities of millions of the halo objects [16], opens a new way to study the origin and evolution of the galactic halo, including globular clusters [17,18], stellar streams [19,20] and satellite galaxies [21,22].

Based on the last data releases, attempts were made to decipher the nature of globular clusters in the Milky Way using the energy–vertical angular momentum space (L_z, E) , where E is a total energy and L_z is the component of the angular momentum of a cluster in the direction perpendicular to the galactic disk. Such attempts were made under the assumption that these objects have values for the energy and z -component of the angular momentum close to the parent accretion event. This idea, proposed by Helmi and de Zeeuw [23], is based on the assumption that the clusters conserve (L_z, E) for billions of years after their accretion onto our galaxy. This picture assumes that the galactic potential was static during billions of years of galactic evolution. In addition, the authors did not take into account such effects as the dynamical friction, which significantly changes the energy and the angular momentum of the satellite during its accretion, and the influence of the Milky Way’s elongated bar/bulge potential, which may affect the positions of the clusters on the (L_z, E) -plane, especially for those clusters that have small pericentric radii.

The aforementioned (L_z, E) classification approach allowed researchers to detect several merger events of the satellite galaxies, such as GSE [6,11], Sequoia [24], Sagittarius [5], Kraken [25] and Pontus [26,27]. However, Pagnini et al. [28], using dissipation-less N-body simulations that reproduce the accretion of one or two satellites with their globular cluster population on a Milky Way-type galaxy, it was found that accreted globular clusters do not show dynamical coherence; that is, they do not concentrate in kinematic spaces, if the mass of the progenitor satellite galaxy is approximately about 10% of the mass of the Milky Way. This seems quite contrary to the identification methods presented above. However, for small accreted satellite galaxies, accretion products (globular clusters) can be confined in a tight range of energies and momentum. In this case, other mechanisms (in particular galactic bar) may alter the identification of clusters in the same accretion event.

Malhan et al. [26] used the extended approach and determined the action angles $J = (J_R, J_\phi, J_z)$ for known globular clusters, together with their total energies E . By analysing the distributions of the clusters in $(J_\phi = L_z, E)$, (J_R, E) , (J_z, E) and $(J_\phi = L_z, J_R)$, the authors concluded that clusters with similar values of these quantities belong to the same accretion event.

The Milky Way potential, however, is neither stationary nor axisymmetric. In the central parts, the Milky Way potential is influenced by the non-axisymmetric and non-stationary potential of the galactic bar, so the dynamics of the clusters that have small enough pericentric distances will be strongly affected by bar potential after a few passages. In addition, the positions and the velocities of the clusters are determined with errors, which also can significantly affect the identification of the clusters in (L_z, E) -space. It should be noted here, that we will limit ourselves to studying only (L_z, E) -space, because the calculation of J_R and J_z values in the non-axisymmetric and time-dependent potential with elongated bar/bulge component is not possible. Since the Hamiltonian becomes time-dependent, canonical transformation to action-angle coordinates cannot be obtained [29].

In this paper, we study the combined influence of the Milky Way bar potential and the observational errors to test the identification of GSE and Pontus as two different accretion events Malhan et al. [26]. We recall that the significant influence of the bar on the orbits of objects has been shown in the many previous studies: for globular clusters in Chemel et al. [30]; for stellar streams in Hattori et al. [31] and Hunt and Bovy [32]. Accordingly, the layout of the paper is as follows. Section 2 describes available observational data for the globular clusters of the Milky Way halo; Section 3 discusses the model we adopted to study the dynamics of a globular cluster in Milky Way axisymmetric and non-axisymmetric

Table 1. Heliocentric parameters of globular clusters.

Name	R.A. (deg)	Decl. (deg)	D_{\odot} (kpc)	v_{los} (km s $^{-1}$)	μ_{α}^* (mas yr $^{-1}$)	μ_{δ} (mas yr $^{-1}$)
1	2	3	4	5	6	7
Pontus clusters:						
NGC 6341/M 92	259.281	43.136	8.50 (0.07)	-120.55 (0.27)	-4.9349 (0.0243)	-0.6251 (0.0239)
NGC 6779/M 56	289.148	30.183	10.43 (0.14)	-136.97 (0.45)	-2.0179 (0.0251)	1.6176 (0.0252)
NGC 6205/M 13	250.422	36.460	7.42 (0.08)	-244.90 (0.30)	-3.1493 (0.0227)	-2.5735 (0.0231)
NGC 7099/M 30	325.092	-23.180	8.46 (0.09)	-185.19 (0.17)	-0.7374 (0.0246)	-7.2987 (0.0244)
NGC 5286	206.612	-51.374	11.10 (0.14)	62.38 (0.40)	0.1984 (0.0255)	-0.1533 (0.0253)
NGC 288	13.188	-26.583	8.99 (0.09)	-44.45 (0.13)	4.1641 (0.0241)	-5.7053 (0.0243)
NGC 362	15.809	-70.849	8.83 (0.10)	223.12 (0.28)	6.6935 (0.0245)	-2.5354 (0.0242)
tentative cluster:						
NGC 6864/M 75	301.520	-21.921	20.52 (0.45)	-189.08 (1.12)	-0.5975 (0.0262)	-2.8099 (0.0258)
Gaia-Sausage/Enceladus clusters:						
NGC 6229	251.745	47.528	30.11 (0.47)	-137.89 (0.71)	-1.1706 (0.0263)	-0.4665 (0.0267)
NGC 7492	347.111	-15.611	24.39 (0.57)	-176.70 (0.27)	0.7558 (0.0279)	-2.3200 (0.0276)
NGC 6584	274.657	-52.216	13.61 (0.17)	260.64 (1.58)	-0.0898 (0.0258)	-7.2021 (0.0254)
NGC 5634	217.405	-5.976	25.96 (0.62)	-16.07 (0.60)	-1.6918 (0.0269)	-1.4781 (0.0263)
IC 1257	261.785	-7.093	26.59 (1.43)	-137.97 (2.04)	-1.0069 (0.0400)	-1.4916 (0.0321)
NGC 1851	78.528	-40.047	11.95 (0.13)	321.40 (1.55)	2.1452 (0.0240)	-0.6496 (0.0242)
NGC 2298	102.248	-36.005	9.83 (0.17)	147.15 (0.57)	3.3195 (0.0255)	-2.1755 (0.0256)
NGC 4147	182.526	18.543	18.54 (0.21)	179.35 (0.31)	-1.7070 (0.0273)	-2.0896 (0.0274)
NGC 1261	48.068	-55.216	16.40 (0.19)	71.34 (0.21)	1.5957 (0.0249)	-2.0642 (0.0251)
NGC 6981/M 72	313.365	-12.537	16.66 (0.18)	-331.39 (1.47)	-1.2736 (0.0262)	-3.3608 (0.0257)
NGC 1904/M 79	81.044	-24.524	13.08 (0.18)	205.76 (0.20)	2.4690 (0.0249)	-1.5938 (0.0251)
NGC 7089/M 2	323.363	-0.823	11.69 (0.11)	-3.78 (0.30)	3.4346 (0.0247)	-2.1588 (0.0244)
NGC 5904/M 5	229.638	2.081	7.48 (0.06)	53.50 (0.25)	4.0856 (0.0230)	-9.8696 (0.0231)

time-dependent potentials. Section 4 describes the our results of evolution of the globular clusters in (L_z, E) space. Section 5 summarises the results of our study.

2. Observational Data

To demonstrate the influence of the galactic bar on the positions of the globular clusters on the (L_z, E) diagram, we selected two groups of globular clusters that were identified in the literature as the members of two progenitor dwarf galaxies—Pontus and GSE [26,27]. The Pontus group consists of seven globular clusters, and the GSE group consists of 13 clusters listed in Table 1. In addition, we include in our considerations the tentative globular cluster NGC 6864/M 75, indicated by Malhan et al. [26] as a possible candidate for both groups of globular clusters. Table 1 provides parameters of the globular clusters, together with their observational errors (inside the parentheses) taken from [17,18].

1—name of globular cluster; 2—right ascension (R.A.); 3—declination (Decl.); 4—heliocentric distance (D_{\odot}); 5—spectroscopic line-of-sight velocities (v_{los}); 6, 7—proper motions ($\mu_{\alpha}^* = \mu_{\alpha} \cos \delta$, μ_{δ}); the values in parentheses represent observational errors.

To convert the heliocentric measurements provided in Table 1 into the values in the Galactocentric reference frame, the *astropy* package [33–35] was used. We adopted for the solar Galactocentric distance the value of $R_{\odot} = 8.122$ kpc taken from GRAVITY Collaboration et al. [36], and for the velocity components of the Sun, the values of $V_{\odot} = (12.9, 245.6, 7.78)$ km/s taken from Drimmel and Poggio [37], Reid and Brunthaler [38]. The displacement of the Sun from the mid-plane of the Galaxy, the value $Z_{\odot} = 20.8$ pc was taken from Bennett and Bovy [39].

Figure 1 shows the positions of the globular clusters on the angular momentum–energy plane (L_z, E) , calculated with the axisymmetric galactic potential *McMillan17* using data taken from Table 1. The potential model is described in more detail in Section 3. Figure 1 shows also the influences of the observational errors on the positions of the globular clusters on the

(L_z, E) -plane calculated using one hundred randomly chosen coordinates, consistent with the errors in Table 1 (inside the parentheses). We have assumed a normal distribution with the standard deviations set by the errors.

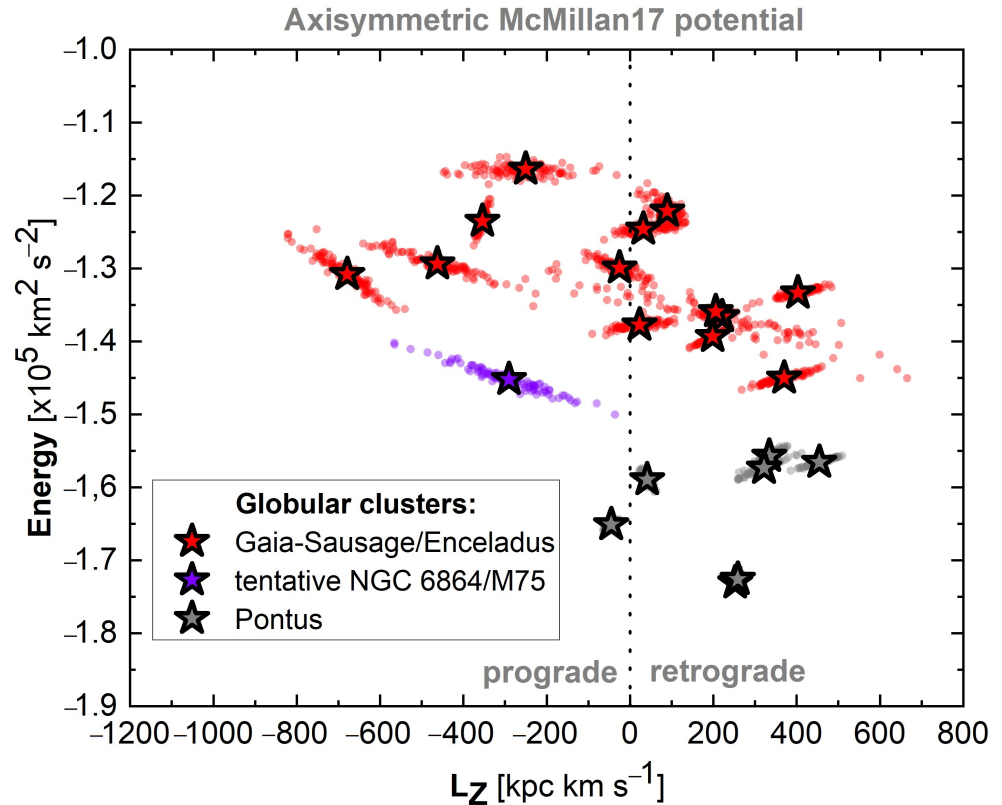


Figure 1. Positions of the globular clusters in the (L_z, E) -plane. Asterisks mark the mean values of L_z and E . Red—GSE; grey—Pontus globular clusters; purple— the tentative NGC 6864/M 75 cluster. The dots show one hundred randomly chosen globular cluster locations consistent with the errors in Table 1. We have assumed a normal distribution with the standard deviations set by the errors.

As one can readily see in Figure 1, Pontus objects have z-components of the angular momentum within $L_z \sim [-50, 500] \text{ kpc km s}^{-1}$ and energies within $E \sim [-1.75, -1.55] \times 10^5 \text{ km}^2 \text{ s}^{-2}$. These values are systematically lower compared to the energies of the GSE group, which have the values of $E \sim [-1.45, -1.15] \times 10^5 \text{ km}^2 \text{ s}^{-2}$ and $L_z \sim [-900, 700] \text{ kpc km s}^{-1}$. Based on these differences, Malhan et al. [26] came to the conclusion that these groups of clusters belong to different merger events. Besides the values $L_z = J_\phi$ and E , Malhan et al. [26] considered the action-angles J_R and J_z as well. In this study, we refrained from this procedure, since the calculation of these values in a non-axisymmetric and time-dependent potential is not possible. We will instead focus our efforts on the influence of the galactic bar/bulge on evolution of the objects on the (L_z, E) -plane. We notice that all objects listed in Table 1 have small pericentric radii ($r_{peri} < 3 \text{ kpc}$), which makes a strong influence of the bar on these objects. We notice also that the globular clusters from Table 1 have both prograde and retrograde orbits, which is caused, probably, by the internal velocity dispersion of globular clusters that were accreted almost radially on the Milky Way galaxy [26,27].

3. The Models

We conducted simulations of the dynamics of the globular clusters using the astrophysical package `Galpy` [40]. The integration of orbits was performed using a Dormand-Prince (`dop853`) integrator [41], which is an eighth order Runge–Kutta family method with adaptive timestep. This method was implemented in the package `Galpy`, and for 1000 orbital periods, it conserved energy at the level of $\Delta E/E = 10^{-8}$ in the case of an axisymmetric time-independent potential.

We integrated the orbits during 4 Gyr forward in time starting from the present epoch, supposing that building of Galaxy was stopped approximately 4 Gyr ago [42]. Therefore, the bar potential remained approximately constant during the last 4 Gyr. The simulations show that bar stops its evolution after the thickening phase and remains almost unchanged as long as the calculations are performed [43,44]. Therefore, 4 Gyr is enough time to demonstrate that even with the fixed bar potential, the quantities used to pinpoint the past accretion events are not conserved. It also follows from the above that it remains not important to integrate orbits forward or backward in time if we want to demonstrate the influence of the bar.

3.1. Galactic Potential Models

To study globular cluster dynamics in the Milky Way potential, we used two models. The first model has an axisymmetric and time-independent potential, whereas the second one has a non-axisymmetric time-dependent potential with an elongated bar/bulge.

3.1.1. Axisymmetric Time-Independent Potential

Following Malhan et al. [26], first we modelled the Milky Way using the axisymmetric potential described by McMillan [45](McMillan17). The model included the bulge, the thick and thin stellar disks, two gaseous disks ($H\text{I}$ and H_2) and the dark matter halo.

The axisymmetric bulge potential was described by the density profile from Bissantz and Gerhard [46] and can be represented as:

$$\rho_b = \frac{\rho_{0,b}}{(1 + r'/r_0)^\alpha} \exp\left[-(r'/r_{\text{cut}})^2\right], \quad (1)$$

where $r' = \sqrt{R^2 + (z/q)^2}$; the parameters α and r_0 were equal to 1.8 and 0.075 kpc, respectively; $r_{\text{cut}} = 2.1$ kpc; and the axis ratio q was equal to 0.5. The central volume density of the bulge: $\rho_{0,b} = 9.84 \times 10^{10} M_\odot \text{kpc}^{-3}$, which gives a total bulge mass equal to $M_b = 9.23 \times 10^9 M_\odot$.

The Milky Way disk consists of two subsystems, the thin and the thick [47] exponential disks both described by density profiles with the form:

$$\rho_d(R, z) = \frac{\Sigma_0}{2z_d} \exp\left(-\frac{|z|}{z_d} - \frac{R}{R_d}\right). \quad (2)$$

Here, z_d , R_d and Σ_0 are the vertical scale height, the radial scale length and central surface density, respectively. The vertical scale heights of the disks are fixed to the values $z_{d,\text{thin}} = 300$ pc and $z_{d,\text{thick}} = 900$ pc, and the scale lengths for the thin and thick disks are assumed to be 2.5 kpc and 3.02 kpc, respectively. With the central surface densities of the thin and of the thick disks taken to be $\Sigma_{0,d,\text{thin}} = 896 M_\odot \text{pc}^{-2}$ and $\Sigma_{0,d,\text{thick}} = 183 M_\odot \text{pc}^{-2}$, the total masses of the thin and of thick disks can be estimated as $M_d = 2\pi\Sigma_0 R_d^2$ and equal to $3.518 \times 10^{10} M_\odot$ and $1.048 \times 10^{10} M_\odot$, respectively. A possible central 'hole' in stellar density is not considered.

The McMillan17 potential also includes two gaseous disks: the atomic ($H\text{I}$) one and the molecular (H_2) one. The density distributions in both gaseous disks are described by this equation:

$$\rho_d(R, z) = \frac{\Sigma_0}{4z_d} \exp\left(-\frac{R_m}{R} - \frac{R}{R_d}\right) \text{sech}^2(z/2z_d). \quad (3)$$

Here, R_m gives the scale length of central gaseous hole. For the $H\text{I}$ disk, the following parameters are adopted: $R_{d,H\text{I}} = 7$ kpc, $z_{d,H\text{I}} = 85$ pc, $\Sigma_{0,d,H\text{I}} = 53.1 M_\odot \text{pc}^{-2}$, $R_{m,H\text{I}} = 4$ kpc. For the H_2 gaseous disk, the accepted values are $R_{d,H_2} = 1.5$ kpc, $z_{d,H_2} = 45$ pc, $\Sigma_{0,d,H_2} = 2180 M_\odot \text{pc}^{-2}$ and $R_{m,H_2} = 12$ kpc.

The potential of the dark matter halo is described by the simple density profile given by this equation:

$$\rho_h = \frac{\rho_{0,h}}{x^\gamma (1+x)^{3-\gamma}}, \quad (4)$$

where $x = r/r_h$, and $r_h = 19.6$ kpc is the scale length of the density distribution, and $\rho_{0,b} = 0.00854 \times 10^{10} M_\odot \text{kpc}^{-3}$ is a characteristic scaling density of the halo. With the parameter $\gamma = 1$, Equation (4) becomes a classic NFW [48] density profile. The mass of the dark-matter halo (within the sphere of 200 kpc) is equal to $M_{200} = 1.216 \times 10^{12} M_\odot$.

All parameter values came from McMillan17 [45]. To integrate the equations of motion, it is necessary to calculate the potentials using known density distributions. The NFW potential has analytical representation. The potential of the bulge was calculated using the basis-function expansion of the self-consistent-field method of Hernquist and Ostriker [49]. Potentials for disks were calculated using a modified technique of Hernquist and Ostriker [49], which was presented in Kuijken and Dubinski [50] and implemented in the `Galpy` package [40].

3.1.2. Non-Axisymmetric Time-Dependent Potential with Elongated Bar/Bulge

In this model, we replaced the axisymmetric bulge with the non-axisymmetric elongated bar/bulge component.

Following Chemel et al. [30] and Yeh et al. [51], we approximate the bar/bulge by a rotating ellipsoid with a density distribution given by a Ferrers model [40]:

$$\rho(x, y, z) = \begin{cases} \rho_c(1 - m^2)^2 & , \text{ if } m < 1, \\ 0 & , \text{ if } m > 1, \end{cases} \quad (5)$$

where $m^2 = \frac{x^2}{a^2} + \frac{y^2}{b^2} + \frac{z^2}{c^2}$. For the bar semi-axes, we chose the values $a = 5$ kpc, $b = 2$ kpc and $c = 1$ kpc, which gives a good approximation for the elongated bar/bulge observed in the Milky Way (see, for example, Model M85 in Portail et al. [8,9]). The central density of the bar in this model is determined by the expression $\rho_c = \frac{105}{32\pi} \frac{GM_b}{abc}$, where M_b is the mass of the bar, for which we adopted the value $M_b = 1.88 \times 10^{10} M_\odot$ from Portail et al. [9] (also similar to Kent [52]). Zhao et al. [53] built a self-consistent model of the bar/bulge and found the total mass of the bar taken to be equal $2 \times 10^{10} M_\odot$ [54]. Kipper et al. [55] estimated a smaller value of $\sim 1.6 \times 10^{10} M_\odot$.

The gravitational potential produced by the density in Equation (5) can be [51,56]:

$$\Phi = -\pi Gabc \frac{\rho_c}{n+1} \int_\lambda^\infty \frac{du}{\Delta(u)} (1 - \zeta^2(u))^3, \quad (6)$$

$$\text{where } \zeta^2(u) = \frac{x^2}{a^2 + u} + \frac{y^2}{b^2 + u} + \frac{z^2}{c^2 + u}, \quad (7)$$

$$\text{and } \Delta^2(u) = (a^2 + u)(b^2 + u)(c^2 + u), \quad (8)$$

where n is integer number, which is equal to two, according to the degree in Equation (5). λ is the unique positive solution of $\zeta^2(\lambda) = 1$, outside the bar ($\zeta \geq 1$). Inside the bar, $\lambda = 0$ (for the more details see Pfenniger [56]).

The Milky Way bar rotates with constant angular velocity, and the major axis is tilted with respect to the Sun, as shown in Figure 2.

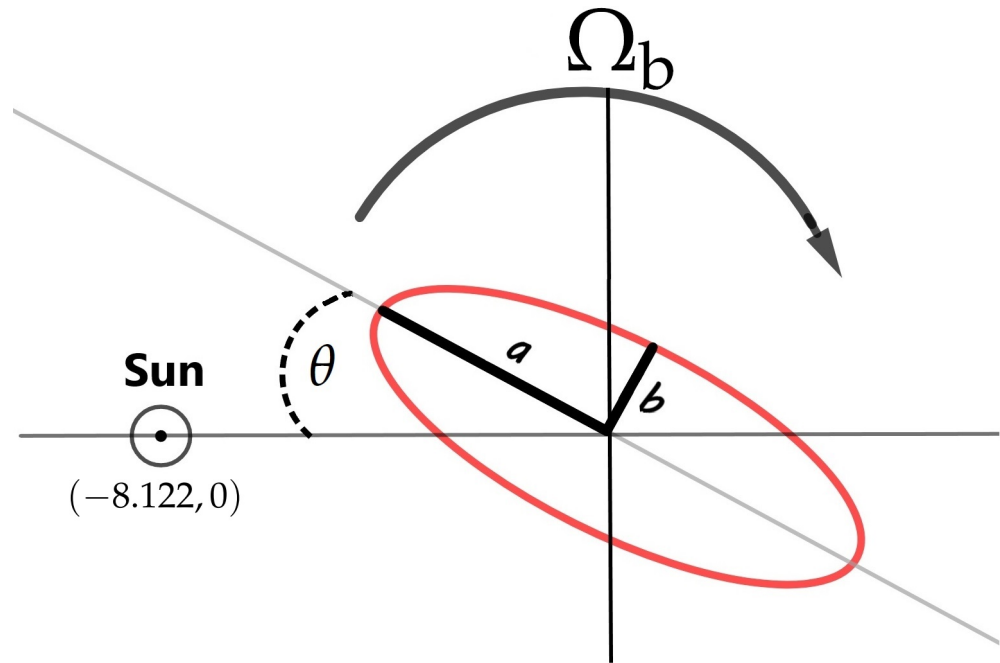


Figure 2. Schematic representation of the position of the Milky Way bar relative to the Sun. The angle θ between the Sun and the bar is 28° . The bar has an angular rotation velocity Ω_b and rotates clockwise, so Ω_b has a negative sign.

A number of studies estimated the bar orientation relative to the Sun ([8,9,54,57,58]) and its angular velocity ([57,59–62]). Debattista et al. [59] were the first to estimate the angular velocity of the galactic bar: $\Omega_b = 59 \pm 5 \text{ km s}^{-1} \text{ kpc}^{-1}$. Recent data that used Gaia proper motion measurements allow one to estimate the pattern speed of the bar more accurately, although the spread in the measurements remains considerable. Sanders et al. [57] using the VVV Infrared Astrometric Catalogue (VIRAC) and Gaia DR2 proper motions obtained the value of $\Omega_b = 41 \pm 3 \text{ km s}^{-1} \text{ kpc}^{-1}$. Clarke et al. [60] obtained $\Omega_b = 37.5 \text{ km s}^{-1} \text{ kpc}^{-1}$ [61]. Sormani et al. [62], using hydrodynamic gas simulations in barred Milky Way potential, found that the angular velocity of the bar is $\Omega_b = 40 \text{ km s}^{-1} \text{ kpc}^{-1}$. We chose in our non-axisymmetric model the value of $\Omega_b = 40 \text{ km s}^{-1} \text{ kpc}^{-1}$, which is in a good agreement with Portail et al. [8,9] and Bovy et al. [63].

Recent measurements of the bar orientation θ relative to the Sun lie in the range of $23^\circ - 33^\circ$ [8,9,54,57]. We used in our simulations the value $\theta = 28^\circ$, which is in a good agreement with the most recent estimates [9,54,58].

3.2. Rotation Curves: Comparison of Axisymmetric and Non-Axisymmetric Models

Figure 3 shows the Milky Way rotation curves in our barred and non-barred models. The model with the bar has systematically higher values of the rotational velocity compared to the axisymmetric model McMillan17 due to the fact that in the model with the bar, we

replaced the axisymmetric bulge in McMillan17 with an elongated bar/bulge whose mass is about two times larger than the mass of the bulge in the McMillan17 model. Rotation curves in Figure 3 were derived (in the plane $z=0$) from the equation $v(r) = (r d\Phi/dr)^{1/2}$, where Φ is the total potential.

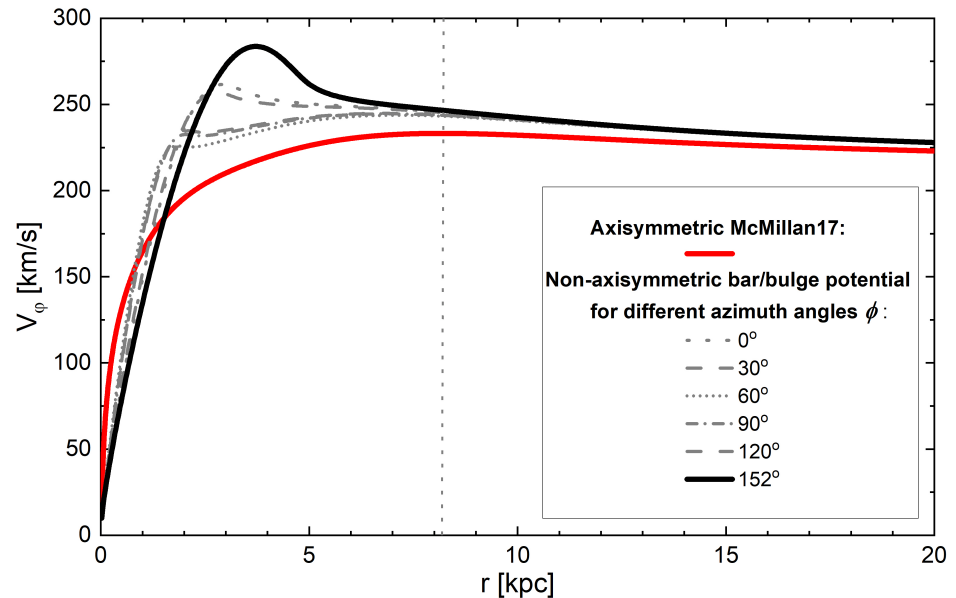


Figure 3. Rotation curves for axisymmetric McMillan17 (red line) and for a non-axisymmetric model with the bar for different orientations (black lines). Angle of 152° corresponds to the direction along the major axis of the bar.

4. Results and Discussion

We discuss in this section the dynamics of the halo globular clusters and the influence of the galactic bar on their positions in the (L_z, E) -plane.

Figure 4 shows the (L_z, E) -positions of the globular clusters calculated using data taken from Table 1 for barred and non-barred galactic potential models. Figure 4 also shows one hundred alternative positions of each cluster considering observational errors. As one can readily see, the clusters have similar values of L_z and E with minor differences. Note, however, that while in the axisymmetric and time-independent potential, the values of L_z and E are conserved, in time-dependent non-axisymmetric potential, these values are not conserved in time. We will discuss in detail the non-conservation of L_z and E below.

First, let us consider the influence of the galactic bar on the positions of the clusters on (L_z, E) -plane using mean values of their parameters (asterisks in Figure 4) in time-dependent non-axisymmetric potential.

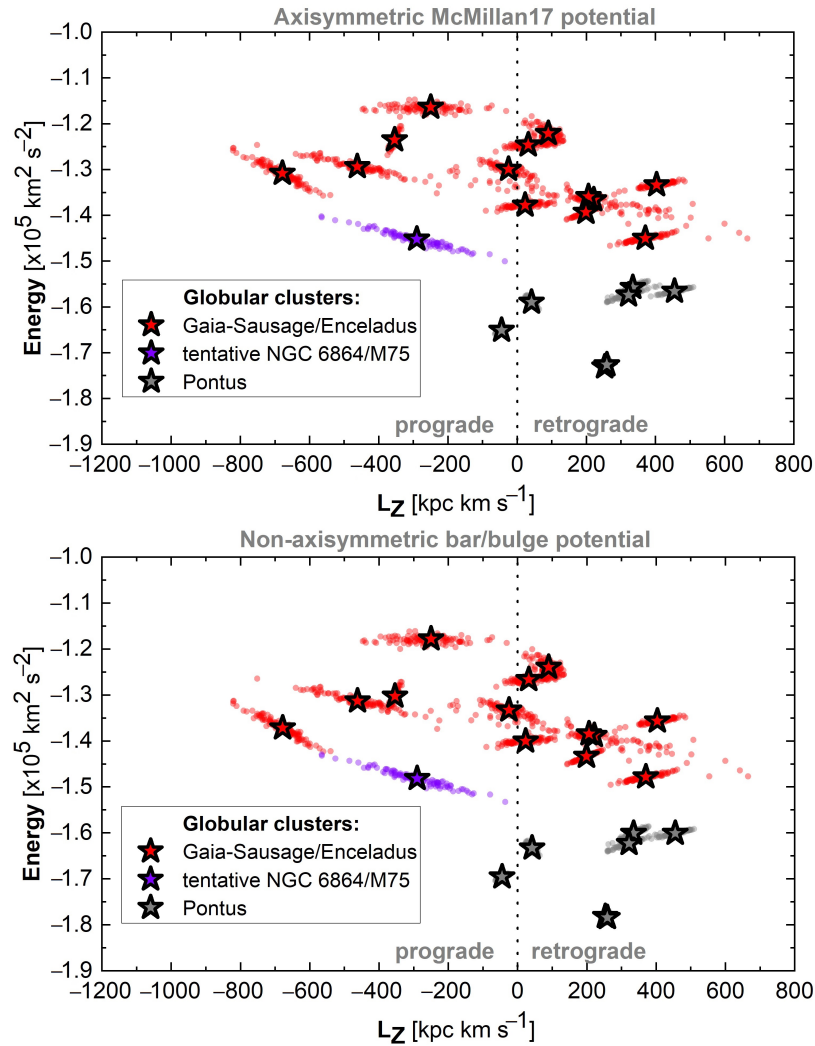


Figure 4. Positions of the globular clusters on the (L_z, E) -plane for two galactic potential models, the axisymmetric model of McMillan17 (top panel) and a non-axisymmetric model (bottom panel). Asterisks mark the mean values of L_z and E on the plane.

To do this, we integrated the orbits of each cluster during 4 Gyr in the non-axisymmetric potential that includes the rotating bar/bulge. The evolution of each globular cluster on the (L_z, E) -diagram is shown in Figure 5. The initial positions of clusters in (L_z, E) space are indicated in Figure 5 with asterisks. As can be seen in the Figure, in the non-axisymmetric potential of the bar, rotating with the constant angular velocity Ω_b , the clusters oscillate along a straight line that has the same slope for each cluster. This is due to the fact that in the non-axisymmetric time-dependent potential, the z-component of the angular momentum L_z and the total energy E of the object are not conserved. Instead, the Jacobi integral described by the equation:

$$E_j = E - \Omega_b L_z. \quad (9)$$

is conserved for each cluster (see, e.g., Hattori et al. [31]). Equation (9) shows that in case of constant angular velocity of the bar, the total energy E is a linear function of L_z , resulting in the clusters oscillating in Figure 5 along parallel lines.

As can be seen in Figure 5, the positions of GSE and Pontus clusters are significantly affected by the Milky Way bar, which blur their positions on the (L_z, E) diagram over time. Energy variation for clusters is up to 15%, and variation of the angular momentum is more than 100%. It should also be noted that some Pontus objects reach energy values of the GSE group.

We then took into account the errors in observational data of coordinates and proper motions, leading to the uncertainties in the initial galactocentric coordinates and the velocities of the the globular clusters. To do this, we randomly generated one hundred sets of the coordinates in the 6D phase space for each globular cluster. They were drawn assuming Gaussian errors in the measured coordinates and velocities, and then we calculated the positions of the clusters on the (L_z, E) -plane.

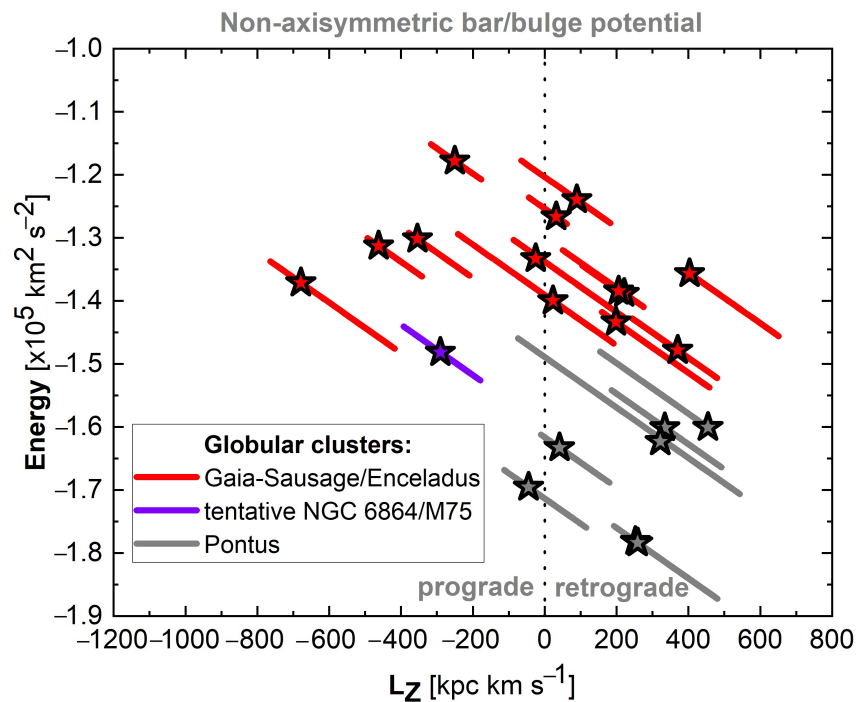


Figure 5. Evolution of the globular clusters on the (L_z, E) -plane for non-axisymmetric potential with the rotating bar. Asterisks mark the initial positions of the clusters in the L_z, E -plane (red colour—GSE objects; grey—Pontus objects; purple—tentative NGC 6864/M 75 cluster). The lines show trajectories along which the globular clusters oscillate.

Before discussing the evolution of the globular clusters on the (L_z, E) -plane, a closer look at the dynamics of one globular cluster in the Pontus group—NGC 288—is necessary. Figure 6 shows time dependence of the angular momentum L_z and the total energy E for the mean values of the initial conditions (red line), while also taking into account observational errors (100 grey dotted lines). As one can see, the angular momentum and the energy of the cluster are significantly affected by the time-dependent potential of the rotating bar. The values oscillate with time and correlate with each other according to Equation (9). The stepwise changes in momentum and energy are due to the moments of time when the cluster comes close to the bar and passes through it. Areas with almost constant values refer to the moments in time when the cluster was moving far from the bar. Observational errors spread the values of the angular momentum and the energy of the cluster. After only 1–2 Gyr of evolution, the range of values consistent with the observational error is quite large. The spread of the

values of the angular momentum is within $L_z \sim [-0, 600] \text{ kpc km s}^{-1}$, and total energy of the cluster gets the values $E \sim [-1.70, -1.42] \times 10^5 \text{ km}^2 \text{ s}^{-2}$. For comparison, the black dotted lines in Figure 6 showed the constant values of L_z and E in the time-independent axisymmetric potential of McMillan17.

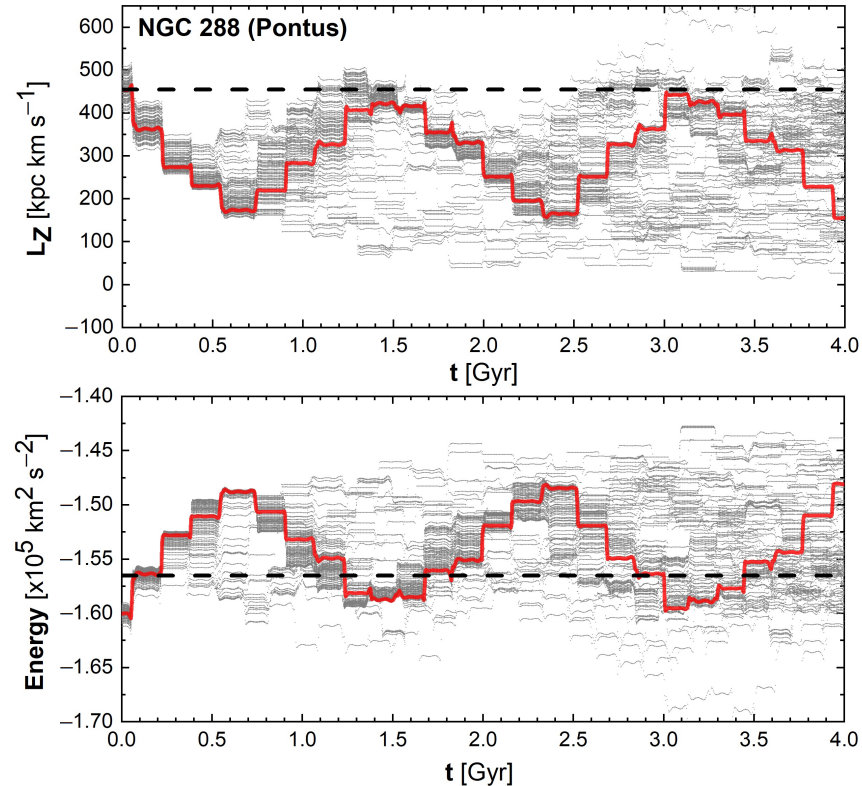


Figure 6. Evolution of the total energy E (bottom frame) and the z -component of angular momentum L_z (upper frame) for the globular cluster NGC 288 evolving in the non-axisymmetric rotating potential of the bar. The red line shows the evolution for the mean value of initial conditions. The grey lines are one hundred representations of the orbits taking into account the observational errors in coordinates and proper motions. The black dashed line shows the constant angular momentum and energy in the axisymmetric McMillan17 potential. Time $t = 0$ means the start time of the simulation and corresponds to the present time.

Figure 7 shows the three-dimensional orbits of the globular cluster NGC 288 in the axisymmetric potential McMillan17 and in the non-axisymmetric potential with the rotating bar. Figure 8 shows the orbits of the cluster projected onto the three galactocentric planes. The mean orbits are shown as red lines, whereas one hundred alternative orbits consistent with the observational errors of these initial conditions are shown in grey. We can see that the bar significantly affects the dynamics of the globular cluster: the bar significantly randomises the orbits and destroys orbital boxes (diagram R vs. z in Figure 8), confirming the significant influence of the bar stressed by Chemel et al. [30] and Hattori et al. [31]. The cluster NGC 288 has a small pericentric distance similar to the other clusters considered in this paper. For the clusters that have larger pericenters, the influence of the bar will obviously decrease due to the increase in the distance of the symmetry of the equipotential surfaces of the bar.

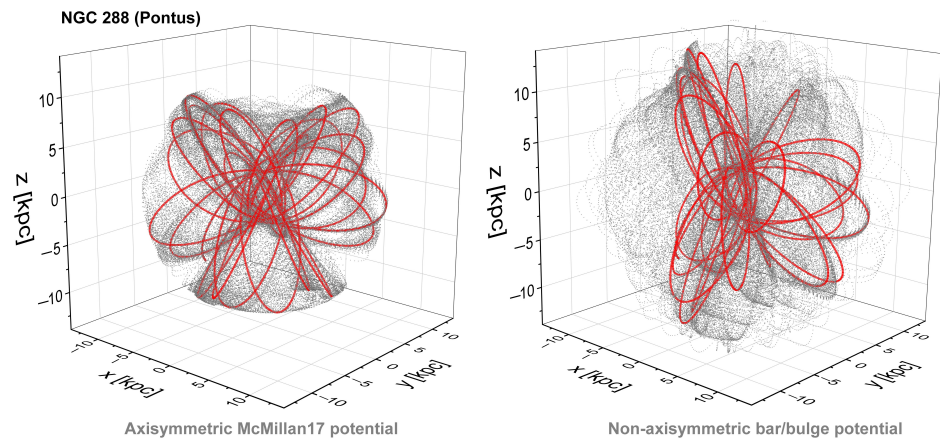


Figure 7. Three-dimensional orbits of globular cluster NGC 288 in the axisymmetric potential McMillan17(left panel) and in the non-axisymmetric rotating bar/bulge potential (right panel). The red lines show the orbits for the mean initial conditions. The grey lines show one hundred orbits consistent with the observational errors in these initial conditions.

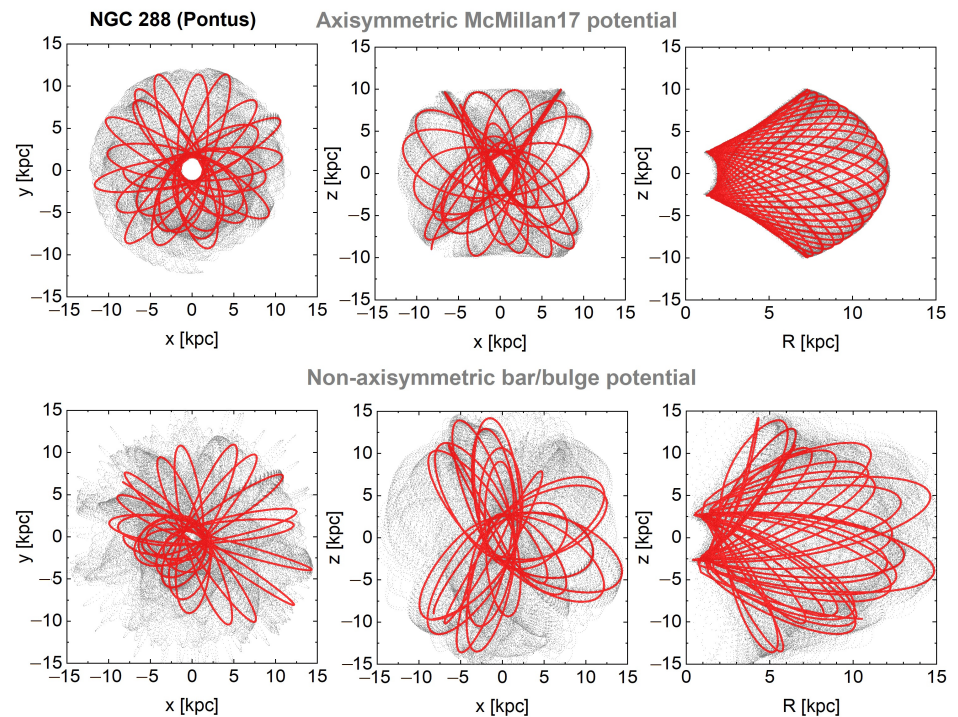


Figure 8. Projections of the cluster orbits onto the galactocentric coordinate planes for the axisymmetric potential McMillan17(top frames) and for the non-axisymmetric potential of the rotating bar (bottom frames). The red lines show the orbit for the mean initial conditions, whereas the grey lines show one hundred orbits consistent with the observational errors in these initial conditions.

McMillan17 (left panel) and the non-axisymmetric rotating bar/bulge potential (right panel): the red lines show the orbits for the mean initial conditions. The grey lines show one hundred orbits consistent with the observational errors in these initial conditions.

Finally, let us consider the joint influence of the bar and of the observational errors on the evolution of the clusters in the (L_z, E) -plane. To do this, we took one hundred representations of the orbits using the errors in Table 1 and represented by dots in Figure 4.

This is illustrated in Figure 9, which shows the evolution of the clusters—represented by one hundred dots for each clusters in Figure 4—in the non-stationary potential of the rotating bar, and under the influence of the uncertainties in the initial kinematical data of the clusters. It is difficult to conclude that these clusters belong to two different accretion events, namely, Pontus and GSE, as was suggested by Malhan et al. [26]. The "tentative" cluster NGC 6864 overlaps with both groups. Thus, it cannot be concluded that GSE and Pontus clusters belong to different accretion events and so to different progenitor galaxies. The same can be said about the origin of the tentative object NGC 6864. It is also impossible to make firm conclusion on which group the tentative object NGC 6864 belongs to.

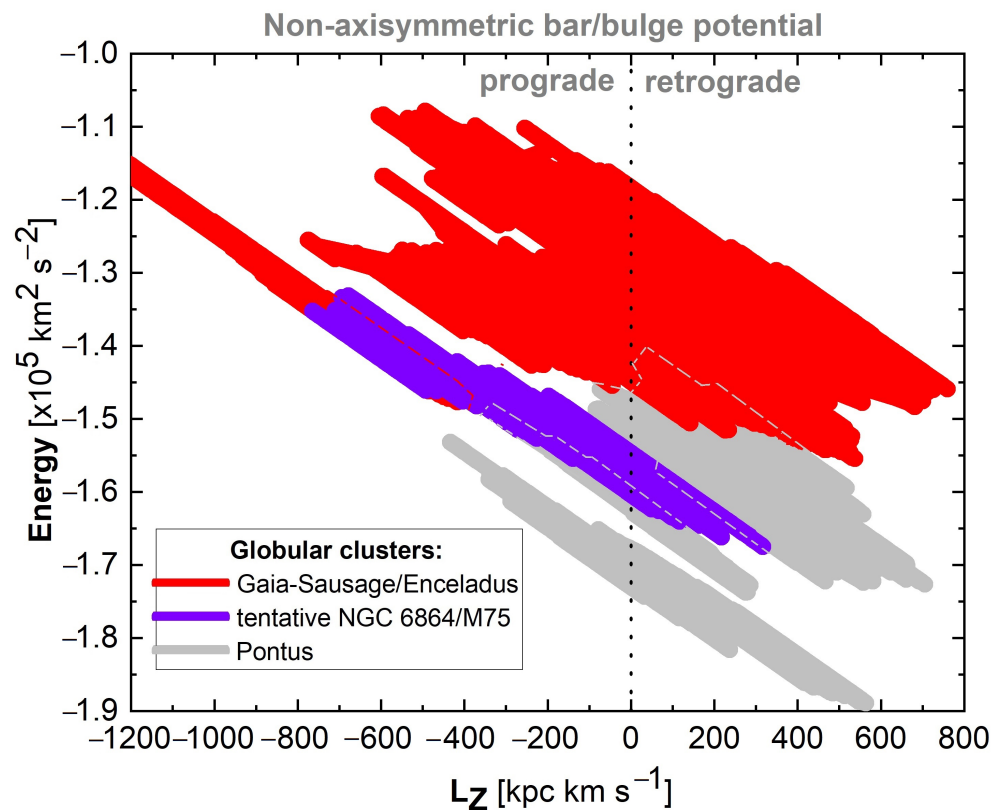


Figure 9. Evolution of the globular clusters from Table 1 during 4 Gyr after the beginning of simulations, taking into account the non-axisymmetric potential of the rotating bar and the observational errors of the initial conditions.

In more general terms, we conclude that it is difficult to identify accretion events using objects that have close passages around the galactic centre. For those objects, the bar significantly affects the values of E and L_z . One should also take into account that during accretion of a dwarf galaxy, dynamical friction constantly changes its energy and momentum, making the identification of the original accretion events even more difficult.

Finally, we did not take into account the influence of other important physical phenomena that can also affect the positions of the clusters on the L_z, E -diagram such as the change of the galactic potential due to galaxy's accretion and secular evolution, the change of the angular

velocity of bar during its evolution, the influence of the spiral structure, and the interaction of globular clusters with satellite galaxies on evolution of the globular clusters. We will attempt to include the effect of these phenomena in the future.

5. Summary

In this study, we concluded that the bar significantly affects the dynamics of the globular clusters with small enough pericentric distances. We found that the bar potential renders the orbits of such clusters quite chaotic, confirming the results obtained by Chemel et al. [30]. If one takes into account the bar potential and the observational errors in the heliocentric coordinates and in the proper motions of the clusters, it is evident that the positions of the clusters on L_z, E -diagram are not tight anymore, making it impossible to identify the cluster's association with a particular accretion event or progenitor galaxy. This result is especially true for those clusters that pass close enough to the galactic centre and have the perihelion less than about 3 kpc, i.e., where the influence of the bar is stronger. To stress it yet again, in this work we provided strong evidence that a proper accounting of the influence of the bar, together with observational errors, is mandatory. We have applied this to two particular accretion events—the GSE and the Pontus—and clearly showed that it is impossible to discriminate among different parent merger events.

Author Contributions: Conceptualisation, V.K., G.C. and R.T.; methodology, V.K., G.C. and R.T.; software, R.T., A.J. and B.J.; writing—original draft preparation, R.T., V.K. and G.C.; writing—review and editing, R.T., V.K., A.J., G.C. and B.J. All authors have read and agreed to the published version of the manuscript.

Funding: RT thanks the Foundation for the Advancement of Theoretical Physics and Mathematics 'BASIS' for financial support at <https://basis-foundation.ru>, accessed on 1 July 2022.

Institutional Review Board Statement: Not applicable.

Informed Consent Statement: Not applicable.

Data Availability Statement: All data used in this paper were taken from the open sources, and the references are given.

Acknowledgments: We thank the anonymous reviewers for the careful reading of the article and valuable comments.

Conflicts of Interest: The authors declare no conflict of interests.

Abbreviations

Abbreviations

The following abbreviations are used in this manuscript:

GSE Gaia-Sausage/Enceladus
NFW Navarro–Frenk–White

References

1. Amorisco, N.C. On feathers, bifurcations and shells: The dynamics of tidal streams across the mass scale. *MNRAS* **2015**, *450*, 575–591. <https://doi.org/10.1093/mnras/stv648>.
2. Chang, J.; Yuan, Z.; Xue, X.X.; Simion, I.T.; Kang, X.; Li, T.S.; Zhao, J.K.; Zhao, G. Is NGC 5824 the Core of the Progenitor of the Cetus Stream? *ApJ* **2020**, *905*, 100. <https://doi.org/10.3847/1538-4357/abc338>.
3. Dekel, A.; Birnboim, Y.; Engel, G.; Freundlich, J.; Goerdt, T.; Mumcuoglu, M.; Neistein, E.; Pichon, C.; Teyssier, R.; Zinger, E. Cold streams in early massive hot haloes as the main mode of galaxy formation. *Nature* **2009**, *457*, 451–454. <https://doi.org/10.1038/nature07648>.

4. Naidu, R.P.; Conroy, C.; Bonaca, A.; Zaritsky, D.; Weinberger, R.; Ting, Y.S.; Caldwell, N.; Tacchella, S.; Han, J.J.; Speagle, J.S.; et al. Reconstructing the Last Major Merger of the Milky Way with the H3 Survey. *ApJ* **2021**, *923*, 92. <https://doi.org/10.3847/1538-4357/ac2d2d>.
5. Ibata, R.A.; Gilmore, G.; Irwin, M.J. A dwarf satellite galaxy in Sagittarius. *Nature* **1994**, *370*, 194–196. <https://doi.org/10.1038/370194a0>.
6. Belokurov, V.; Erkal, D.; Evans, N.W.; Koposov, S.E.; Deason, A.J. Co-formation of the disc and the stellar halo. *MNRAS* **2018**, *478*, 611–619. <https://doi.org/10.1093/mnras/sty982>.
7. Besla, G.; Kallivayalil, N.; Hernquist, L.; Robertson, B.; Cox, T.J.; van der Marel, R.P.; Alcock, C. Are the Magellanic Clouds on Their First Passage about the Milky Way? *ApJ* **2007**, *668*, 949–967. <https://doi.org/10.1086/521385>.
8. Portail, M.; Wegg, C.; Gerhard, O.; Martinez-Valpuesta, I. Made-to-measure models of the Galactic box/peanut bulge: Stellar and total mass in the bulge region. *MNRAS* **2015**, *448*, 713–731. <https://doi.org/10.1093/mnras/stv058>.
9. Portail, M.; Gerhard, O.; Wegg, C.; Ness, M. Dynamical modelling of the galactic bulge and bar: The Milky Way's pattern speed, stellar and dark matter mass distribution. *MNRAS* **2017**, *465*, 1621–1644. <https://doi.org/10.1093/mnras/stw2819>.
10. Carollo, D.; Beers, T.C.; Lee, Y.S.; Chiba, M.; Norris, J.E.; Wilhelm, R.; Sivarani, T.; Marsteller, B.; Munn, J.A.; Bailer-Jones, C.A.L.; et al. Two stellar components in the halo of the Milky Way. *Nature* **2008**, *451*, 216. <https://doi.org/10.1038/nature06542>.
11. Helmi, A.; Babusiaux, C.; Koppelman, H.H.; Massari, D.; Veljanoski, J.; Brown, A.G.A. The merger that led to the formation of the Milky Way's inner stellar halo and thick disk. *Nature* **2018**, *563*, 85–88. <https://doi.org/10.1038/s41586-018-0625-x>.
12. Perryman, M.A.C.; de Boer, K.S.; Gilmore, G.; Høg, E.; Lattanzi, M.G.; Lindegren, L.; Luri, X.; Mignard, F.; Pace, O.; de Zeeuw, P.T. GAIA: Composition, formation and evolution of the Galaxy. *A&A* **2001**, *369*, 339–363. <https://doi.org/10.1051/0004-6361/20010085>.
13. Lindegren, L.; Lammers, U.; Bastian, U.; Hernández, J.; Klioner, S.; Hobbs, D.; Bombrun, A.; Michalik, D.; Ramos-Lerate, M.; Butkevich, A.; et al. Gaia Data Release 1. Astrometry: One billion positions, two million proper motions and parallaxes. *A&A* **2016**, *595*, A4. <https://doi.org/10.1051/0004-6361/201628714>.
14. Fabricius, C.; Bastian, U.; Portell, J.; Castañeda, J.; Davidson, M.; Hambly, N.C.; Clotet, M.; Biermann, M.; Mora, A.; Busonero, D.; et al. Gaia Data Release 1. Pre-processing and source list creation. *A&A* **2016**, *595*, A3. <https://doi.org/10.1051/0004-6361/201628643>.
15. Evans, D.W.; Riello, M.; De Angeli, F.; Carrasco, J.M.; Montegriffo, P.; Fabricius, C.; Jordi, C.; Palaversa, L.; Diener, C.; Busso, G.; et al. Gaia Data Release 2. Photometric content and validation. *A&A* **2018**, *616*, A4. <https://doi.org/10.1051/0004-6361/201832756>.
16. Wu, Y.; Valluri, M.; Panithanpaisal, N.; Sanderson, R.E.; Freese, K.; Wetzel, A.; Sharma, S. Using action space clustering to constrain the recent accretion history of Milky Way-like galaxies. *MNRAS* **2022**, *509*, 5882–5901. <https://doi.org/10.1093/mnras/stab3306>.
17. Vasiliev, E.; Baumgardt, H. Gaia EDR3 view on galactic globular clusters. *MNRAS* **2021**, *505*, 5978–6002. <https://doi.org/10.1093/mnras/stab1475>.
18. Baumgardt, H.; Vasiliev, E. Accurate distances to Galactic globular clusters through a combination of Gaia EDR3, HST, and literature data. *MNRAS* **2021**, *505*, 5957–5977. <https://doi.org/10.1093/mnras/stab1474>.
19. Ibata, R.; Malhan, K.; Martin, N.; Aubert, D.; Famaey, B.; Bianchini, P.; Monari, G.; Siebert, A.; Thomas, G.F.; Bellazzini, M.; et al. Charting the Galactic Acceleration Field. I. A Search for Stellar Streams with Gaia DR2 and EDR3 with Follow-up from ESPaDOnS and UVES. *ApJ* **2021**, *914*, 123. <https://doi.org/10.3847/1538-4357/abfcc2>.
20. Li, T.S.; Ji, A.P.; Pace, A.B.; Erkal, D.; Koposov, S.E.; Shipp, N.; Da Costa, G.S.; Cullinane, L.R.; Kuehn, K.; Lewis, G.F.; et al. S⁵: The Orbital and Chemical Properties of One Dozen Stellar Streams. *ApJ* **2022**, *928*, 30. <https://doi.org/10.3847/1538-4357/ac46d3>.
21. Battaglia, G.; Taibi, S.; Thomas, G.F.; Fritz, T.K. Gaia early DR3 systemic motions of Local Group dwarf galaxies and orbital properties with a massive Large Magellanic Cloud. *A&A* **2022**, *657*, A54. <https://doi.org/10.1051/0004-6361/202141528>.
22. McConnachie, A.W.; Venn, K.A. Updated Proper Motions for Local Group Dwarf Galaxies Using Gaia Early Data Release 3. *Res. Notes Am. Astron. Soc.* **2020**, *4*, 229. <https://doi.org/10.3847/2515-5172/abd18b>.
23. Helmi, A.; de Zeeuw, P.T. Mapping the substructure in the Galactic halo with the next generation of astrometric satellites. *MNRAS* **2000**, *319*, 657–665. <https://doi.org/10.1046/j.1365-8711.2000.03895.x>.
24. Myeong, G.C.; Vasiliev, E.; Iorio, G.; Evans, N.W.; Belokurov, V. Evidence for two early accretion events that built the Milky Way stellar halo. *MNRAS* **2019**, *488*, 1235–1247. <https://doi.org/10.1093/mnras/stz1770>.
25. Reina-Campos, M.; Kruijssen, J.M.D.; Pfeffer, J.L.; Bastian, N.; Crain, R.A. Formation histories of stars, clusters, and globular clusters in the E-MOSAICS simulations. *MNRAS* **2019**, *486*, 5838–5852. <https://doi.org/10.1093/mnras/stz1236>.
26. Malhan, K.; Ibata, R.A.; Sharma, S.; Famaey, B.; Bellazzini, M.; Carlberg, R.G.; D'Souza, R.; Yuan, Z.; Martin, N.F.; Thomas, G.F. The Global Dynamical Atlas of the Milky Way Mergers: Constraints from Gaia EDR3-based Orbits of Globular Clusters, Stellar Streams, and Satellite Galaxies. *ApJ* **2022**, *926*, 107. <https://doi.org/10.3847/1538-4357/ac4d2a>.
27. Malhan, K. A New Member of the Milky Way's Family Tree: Characterizing the Pontus Merger of Our Galaxy. *ApJL* **2022**, *930*, L9. <https://doi.org/10.3847/2041-8213/ac67da>.
28. Pagnini, G.; Di Matteo, P.; Khoperskov, S.; Mastrobuono-Battisti, A.; Haywood, M.; Renaud, F.; Combes, F. The distribution of globular clusters in kinematic spaces does not trace the accretion history of the host galaxy. *arXiv* **2022**, arXiv:2210.04245.
29. Binney, J.; Tremaine, S. *Galactic Dynamics*; Princeton University Press: Princeton, NJ, USA, 2011; Volume 20.

30. Chemel, A.A.; Glushkova, E.V.; Dambis, A.K.; Rastorguev, A.S.; Yalyalieva, L.N.; Klinichev, A.D. Globular Clusters: Absolute Proper Motions and Galactic Orbits. *Astrophys. Bull.* **2018**, *73*, 162–177. <https://doi.org/10.1134/S1990341318020049>.
31. Hattori, K.; Erkal, D.; Sanders, J.L. Shepherding tidal debris with the Galactic bar: The Ophiuchus stream. *MNRAS* **2016**, *460*, 497–512. <https://doi.org/10.1093/mnras/stw1006>.
32. Hunt, J.A.S.; Bovy, J. The 4:1 outer Lindblad resonance of a long-slow bar as an explanation for the Hercules stream. *MNRAS* **2018**, *477*, 3945–3953. <https://doi.org/10.1093/mnras/sty921>.
33. Astropy Collaboration.; Robitaille, T.P.; Tollerud, E.J.; Greenfield, P.; Droettboom, M.; Bray, E.; Aldcroft, T.; Davis, M.; Ginsburg, A.; Price-Whelan, A.M.; et al. Astropy: A community Python package for astronomy. *A&A* **2013**, *558*, A33. <https://doi.org/10.1051/0004-6361/201322068>.
34. Astropy Collaboration.; Price-Whelan, A.M.; Sipőcz, B.M.; Günther, H.M.; Lim, P.L.; Crawford, S.M.; Conseil, S.; Shupe, D.L.; Craig, M.W.; Dencheva, N.; et al. The Astropy Project: Building an Open-science Project and Status of the v2.0 Core Package. *AJ* **2018**, *156*, 123. <https://doi.org/10.3847/1538-3881/aabc4f>.
35. Astropy Collaboration.; Price-Whelan, A.M.; Lim, P.L.; Earl, N.; Starkman, N.; Bradley, L.; Shupe, D.L.; Patil, A.A.; Corrales, L.; Brasseur, C.E.; et al. The Astropy Project: Sustaining and Growing a Community-oriented Open-source Project and the Latest Major Release (v5.0) of the Core Package. *ApJ* **2022**, *935*, 167. <https://doi.org/10.3847/1538-4357/ac7c74>.
36. GRAVITY Collaboration.; Abuter, R.; Amorim, A.; Anugu, N.; Bauböck, M.; Benisty, M.; Berger, J.P.; Blind, N.; Bonnet, H.; Brandner, W.; et al. Detection of the gravitational redshift in the orbit of the star S2 near the Galactic centre massive black hole. *A&A* **2018**, *615*, L15. <https://doi.org/10.1051/0004-6361/201833718>.
37. Drimmel, R.; Poggio, E. On the Solar Velocity. *Res. Notes Am. Astron. Soc.* **2018**, *2*, 210. <https://doi.org/10.3847/2515-5172/aaef8b>.
38. Reid, M.J.; Brunthaler, A. The Proper Motion of Sagittarius A*. II. The Mass of Sagittarius A*. *ApJ* **2004**, *616*, 872–884. <https://doi.org/10.1086/424960>.
39. Bennett, M.; Bovy, J. Vertical waves in the solar neighbourhood in Gaia DR2. *MNRAS* **2019**, *482*, 1417–1425. <https://doi.org/10.1093/mnras/sty2813>.
40. Bovy, J. galpy: A python Library for Galactic Dynamics. *ApJS* **2015**, *216*, 29. <https://doi.org/10.1088/0067-0049/216/2/29>.
41. Alexander, R. Solving Ordinary Differential Equations I: Nonstiff Problems (E. Hairer, SP Norsett, and G. Wanner). *SIAM Rev.* **1990**, *32*, 485–486.
42. Griffen, B.F.; Ji, A.P.; Dooley, G.A.; Gómez, F.A.; Vogelsberger, M.; O’Shea, B.W.; Frebel, A. The Caterpillar Project: A Large Suite of Milky Way Sized Halos. *ApJ* **2016**, *818*, 10. <https://doi.org/10.3847/0004-637X/818/1/10>.
43. Sellwood, J.A.; Wilkinson, A. Dynamics of barred galaxies. *Rep. Prog. Phys.* **1993**, *56*, 173–256. <https://doi.org/10.1088/0034-4885/56/2/001>.
44. Pfenniger, D.; Friedli, D. Structure and dynamics of 3D N-body barred galaxies. *A&A* **1991**, *252*, 75–93.
45. McMillan, P.J. The mass distribution and gravitational potential of the Milky Way. *MNRAS* **2017**, *465*, 76–94. <https://doi.org/10.1093/mnras/stw2759>.
46. Bissantz, N.; Gerhard, O. Spiral arms, bar shape and bulge microlensing in the Milky Way. *MNRAS* **2002**, *330*, 591–608. <https://doi.org/10.1046/j.1365-8711.2002.05116.x>.
47. Gilmore, G.; Reid, N. New light on faint stars - III. Galactic structure towards the South Pole and the Galactic thick disc. *MNRAS* **1983**, *202*, 1025–1047. <https://doi.org/10.1093/mnras/202.4.1025>.
48. Navarro, J.F.; Frenk, C.S.; White, S.D.M. A Universal Density Profile from Hierarchical Clustering. *ApJ* **1997**, *490*, 493–508. <https://doi.org/10.1086/304888>.
49. Hernquist, L.; Ostriker, J.P. A Self-consistent Field Method for Galactic Dynamics. *ApJ* **1992**, *386*, 375. <https://doi.org/10.1086/171025>.
50. Kuijken, K.; Dubinski, J. Nearly Self-Consistent Disc / Bulge / Halo Models for Galaxies. *MNRAS* **1995**, *277*, 1341. <https://doi.org/10.1093/mnras/277.4.1341>.
51. Yeh, F.C.; Carraro, G.; Korchagin, V.I.; Pianta, C.; Ortolani, S. The origin of globular cluster FSR 1758. *A&A* **2020**, *635*, A125. <https://doi.org/10.1051/0004-6361/201937093>.
52. Kent, S.M. Galactic Structure from the Spacelab Infrared Telescope. III. A Dynamical Model for the Milky Way Bulge. *ApJ* **1992**, *387*, 181. <https://doi.org/10.1086/171070>.
53. Zhao, H.; Spergel, D.N.; Rich, R.M. Signature of Bulge Triaxiality From Kinematics in Baade’s Window. *AJ* **1994**, *108*, 2154. <https://doi.org/10.1086/117227>.
54. Bland-Hawthorn, J.; Gerhard, O. The Galaxy in Context: Structural, Kinematic, and Integrated Properties. *ARA&A* **2016**, *54*, 529–596. <https://doi.org/10.1146/annurev-astro-081915-023441>.
55. Kipper, R.; Tenjes, P.; Tuvikene, T.; Ganeshiah Veena, P.; Tempel, E. Quantifying torque from the Milky Way bar using Gaia DR2. *MNRAS* **2020**, *494*, 3358–3367. <https://doi.org/10.1093/mnras/staa929>.
56. Pfenniger, D. The 3D dynamics of barred galaxies. *A&A* **1984**, *134*, 373–386.
57. Sanders, J.L.; Smith, L.; Evans, N.W.; Lucas, P. Transverse kinematics of the Galactic bar-bulge from VVV and Gaia. *MNRAS* **2019**, *487*, 5188–5208. <https://doi.org/10.1093/mnras/stz1630>.

58. Wegg, C.; Gerhard, O. Mapping the three-dimensional density of the Galactic bulge with VVV red clump stars. *MNRAS* **2013**, *435*, 1874–1887. <https://doi.org/10.1093/mnras/stt1376>.
59. Debattista, V.P.; Gerhard, O.; Sevenster, M.N. The pattern speed of the OH/IR stars in the Milky Way. *MNRAS* **2002**, *334*, 355–368. <https://doi.org/10.1046/j.1365-8711.2002.05500.x>.
60. Clarke, J.P.; Wegg, C.; Gerhard, O.; Smith, L.C.; Lucas, P.W.; Wylie, S.M. The Milky Way bar/bulge in proper motions: A 3D view from VIRAC and Gaia. *MNRAS* **2019**, *489*, 3519–3538. <https://doi.org/10.1093/mnras/stz2382>.
61. Shen, J.; Zheng, X.W. The bar and spiral arms in the Milky Way: Structure and kinematics. *Res. Astron. Astrophys.* **2020**, *20*, 159. <https://doi.org/10.1088/1674-4527/20/10/159>.
62. Sormani, M.C.; Binney, J.; Magorrian, J. Gas flow in barred potentials—III. Effects of varying the quadrupole. *MNRAS* **2015**, *454*, 1818–1839. <https://doi.org/10.1093/mnras/stv2067>.
63. Bovy, J.; Leung, H.W.; Hunt, J.A.S.; Mackereth, J.T.; García-Hernández, D.A.; Roman-Lopes, A. Life in the fast lane: A direct view of the dynamics, formation, and evolution of the Milky Way’s bar. *MNRAS* **2019**, *490*, 4740–4747. <https://doi.org/10.1093/mnras/stz2891>.